Synthesis of Iron Oxide Nanoclusters by Thermal Decomposition

Aleksey A. Nikitin,*[†,‡] Igor V. Shchetinin,[†] Natalya Yu. Tabachkova,[†] Mikhail A. Soldatov,[§]
Alexander V. Soldatov,[§] Natalya V. Sviridenkova,[†] Elena K. Beloglazkina,[‡] Alexander G. Savchenko,[†]
Natalya D. Fedorova,[†] Maxim A. Abakumov,*[‡,∥] and Alexander G. Majouga[†,‡,⊥]

[†]National University of Science and Technology "MISIS", Leninskiy prospect 4, 119991 Moscow, Russian Federation
[‡]Department of Chemistry, Lomonosov Moscow State University, Leninskiye gory 1-3, GSP-1, 119991 Moscow, Russian Federation
[§]Southern Federal University, Bolshaya Sadovaya st., 105, 344006 Rostov-on-Don, Russian Federation
[∥]The Russian National Research Medical University, Ostrovityanova 1, 117997 Moscow, Russian Federation
[⊥]Dmitry Mendeleev University of Chemical Technology of Russia, Miusskaya 9, 125047 Moscow, Russian Federation

S Supporting Information

ABSTRACT: Herein, we report a novel one-step solvothermal synthesis of magnetite nanoclusters (MNCs). In this report, we discuss the synthesis, structure, and properties of MNCs and contrast enhancement in T_2-weighted MR images using magnetite nanoclusters. The effect of different organic acids, used as surfactants, on the size and shape of MNCs was investigated. The structure and properties of samples were determined by magnetic measurements, TGA, TEM, HRTEM, XRD, FTIR, and MRI. Magnetic measurements show that obtained MNCs have relatively high saturation magnetization values (65.1−81.5 emu/g) and dependence of the coercive force on the average size of MNCs was established. MNCs were transferred into an aqueous medium by Pluronic F-127, and T_2-relaxivity values were determined. T_2-Weighted MR phantom images clearly demonstrated that such magnetite nanoclusters can be used as contrast agents for MRI.
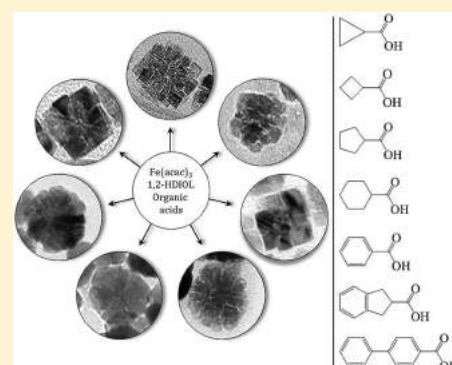
1. INTRODUCTION

The development of nanoparticle-based systems for diagnostic and therapeutic purposes is one of the emerging areas in modern biomedicine. From a number of different nanomaterials, magnetic iron oxide nanoparticles are certainly the most promising material for biomedical applications, including high frequency magnetic field hyperthermia, application as T_2-contrast agents in MRI, application as drug carriers for targeted delivery, cell-labeling, and others.[1,2] The shape is one of the most important factors in determining the biological properties of nanoparticles.[3−5] Shape-controlled synthesis of nanoparticles has become a recent focus, because different shapes of particles can introduce novel magnetic and electric properties, which affect the parameters required for biomedical application, such as MRI and hyperthermia. Much effort has been focused recently on the synthesis of uniform nanoparticles with various shapes, such as spheres and cubes.[6−11]

The first mention about synthesis of iron oxide colloidal nanocrystal clusters was made by the group of S. A. Asher.[12] In this work, polymerization of presynthesized iron oxide nanoparticles in the presence of polystyrene was used to produce iron oxide nanoclusters. A lot of research groups focused their attention on colloidal nanocrystal clusters because the controlled assembly of initial small magnetic nanoparticles into cluster structures with defined shape and size opens horizons for materials which combine properties of individual nanocrystals as well as collective properties due to interactions between the single units. Such iron oxide cluster structures are a very perspective material for various technological and biomedical applications such as separation, catalysis, diagnostics, and treatment of cancer and many others.[13,14]

Many research groups synthesized magnetite nanocrystal clusters with various sizes through thermal decomposition of iron(III) chloride in ethylene glycol with addition of different substances such as sodium and ammonium acetate, polyethylene glycol, ethylenediamine, sodium citrate, poly(acrylic acid) , urea,[15−17] and microclusters.[18−20]

Furthermore, such nanocrystal clusters can be used for MRI application.[21−24] Moreover, in vitro testing and drug delivery with such nanoclusters were performed.[17,24,25] Cho et al. demonstrated that assemblies of iron oxide nanocubes (with an average diameter of 100 nm) exhibited high T_2-relaxivity and heating efficiency.[26]

This paper presents, for the first time, a modified thermal decomposition method that involves self-assembly of magnetite nanoparticles and results in highly ordered cubic or flowerlike magnetite nanoclusters with a controlled size in a suitable for biomedical application size range. The influence of the different

organic acids as surfactants on the shape and size of nanoclusters was investigated. In addition, T_2-weighted MR phantom images clearly demonstrated that such nanoclusters can be used as contrast agents for MRI.

2. EXPERIMENTAL SECTION

2.1. Materials. Iron(III) acetylacetonate (Fe(acac)$_3$; ≥99.9%), benzyl ether (98%), oleic acid (OA; tested according to Ph. Eur.), 1,2-hexadecanediol (1,2-HDIOL; technical grade, 90%), cyclopropane-carboxylic acid (95%), cyclobutanecarboxylic acid (98%), cyclo-pentanecarboxylic acid (99%), cyclohexanecarboxylic acid (98%), benzoic acid (≥99.5%), biphenyl-4-carboxylic acid (95%), ammonium acetate (99.99%), 3-(2-pyridyl)-5,6-diphenyl-1,2,4-triazine-p,p'-disul-fonic acid monosodium salt hydrate (ferrozine; 97%), L-ascorbic acid (≥99.0%), Pluronic F-127, and dichloromethane (≥99.8%) were purchased from Sigma-Aldrich. 1-Indanecarboxylic acid (95%) was purchased from ABCR GmbH & Co. KG. Hexane (≥98.0%), 2-propanol (≥99.8%), and nitric acid (HNO$_3$; ≥65.0%) were purchased from Component-Reaktiv (Moscow, Russia). Hydrochloric acid (HCl; 36%) was purchased from Sigma Tek (Moscow, Russia). All reagents were used without any further purification. Ultrapure Milli-Q water was obtained by means of a Millipore Milli-Q Academic System. All glassware used for synthesis of all samples was cleaned with hot aqua regia (v(HCl)/v(HNO$_3$) = 3/1) and then washed with Milli-Q water.

2.2. General Approach to the Synthesis of MNCs. The mixture of Fe(acac)$_3$ (2 mmol), 1,2-HDIOL (8 mmol), and different organic acids (see Table 1) in benzyl ether (20 mL) was placed in a round-

Table 1. Organic Acids Used for Synthesis of MNCs

Samples \ Acids	A	B	C	D	E	F	G	H	I	J	K	L	M	N
Oleic	▨													
Cyclopropanecarboxylic		▨												
Cyclobutanecarboxylic			▨											
Cyclopentanecarboxylic				▨	▨									
Cyclohexanecarboxylic						▨	▨							
Benzoic								▨	▨	▨				
Biphenyl-4-carboxylic											▨	▨		
1-Indanecarboxylic													▨	▨

bottom flask (50 mL) equipped with a thermometer and a reflux condenser. For removal of oxygen and trace amounts of water from the reaction medium, the solution was warmed up to 130 °C under argon flow and magnetic stirring and maintained for 1 h. Then, the mixture was heated to 210 °C with a rate of about 5 °C/min and kept at this temperature for 1 h. After that, the temperature was raised to 260 °C with a rate of 5 °C/min and kept at this temperature for 30 min. Then, the source of heat was removed and the solution was cooled down to room temperature. MNCs were collected by centrifugation (6000 rpm, 30 min) after adding 10 mL of mixture 2-propanol–hexane (v/v = 1/1). Finally, MNCs were redispersed in dichloromethane (20 mL) and stored at 4 °C.

2.3. Synthesis of Water-Soluble MNCs (MNCs@Pluronic F-127). For transfer of MNCs from organic to aqueous medium, they were conjugated with Pluronic F-127. For this purpose, Pluronic F-127 (1.6 μmol) was dissolved in Milli-Q water (4 mL) and 2 mL of MNCs in dichloromethane ([Fe] = 2.5 mg/mL) was added to this solution. The resulting mixture was heated to 40 °C under argon flow to evaporate the dichloromethane. After that, MNCs@Pluronic F-127 were collected by ultracentrifugation (14 000 rpm) and redispersed in Milli-Q water. This procedure was repeated several times to purify MNCs@Pluronic F-127 from unreacted Pluronic F-127.

2.4. Characterization of MNCs by TEM and HRTEM. Transmission electron microscopy (TEM) images of synthesized MNCs and high-resolution transmission electron microscopy (HRTEM) images were taken on JEOL JEM-1400 (120 kV) and

JEM-2100 (200 kV) microscopes, respectively. All samples were prepared by dropping a dichloromethane dispersion of synthesized samples onto a carbon-coated copper grid (300 mesh) and subsequently evaporating of the solvent. The average diameter of the samples and size distribution were evaluated by using ImageJ software. At least 1000 NPs were analyzed for each sample.

2.5. Characterization of MNCs by XRD Spectroscopy. XRD patterns at room temperature were obtained using an X-ray power diffractometer DRON-4 with Co Kα radiation. The data were collected from 2θ = 20 to 140° at a scan rate of 0.1° per step and 3 s per point. Qualitative phase analysis was performed by comparison of obtained spectra with the PHAN database. Quantitative analysis (including crystal size evaluation by determination of the coherent-scattering region) was performed using PHAN% and SPECTRUM programs developed by Physical Materials Science Department of NUST ≪MISiS≫ (modification of the Rietveld method).

2.6. Characterization of MNCs by Magnetic Measurements. M–H hysteresis loops (from −30 to 30 kOe, 300 K) were obtained on a ≪Quantum Design≫ Physical Property Measurement System (PPMS) equipped with a vibration magnetometric device (VSM) with a 2 mm amplitude of oscillations and 40 Hz frequency.

2.7. Characterization of MNCs by Mössbauer Spectroscopy. Mössbauer spectra of ^{57}Fe nuclei at room temperature were recorded with an MS-1104Em spectrometer in transmission geometry with ^{57}Co(Rh) source of radiation. Spectra analysis was performed by the Univem MS program, and values of effective magnetic fields H_{eff}, isomer shifts δ_s, quadrupole splitting Δ of elementary spectra, and their relative intensity (area) were determined.

2.8. Characterization of MNCs by TGA. Thermogravimetric curves were recorded on a synchronous thermogravimetric analyzer Netzsch STA 449 F3. In a typical procedure, 5 mg of samples was heated in corundum crucibles under argon flow in the temperature range 50–800 °C with a heating rate of 10 °C/min.

2.9. Characterization of MNCs by MRI. The T_2-relaxation rate of water protons in the presence of MNCs covered with Pluronic F-127 was measured in 500 μL test tubes at 18 °C on a ClinScan 7T MRI system. Image acquisition was performed in Spin Echo mode with the following parameters: MRI system TR = 10 000 ms, TE = 8, 16, 24, and 240 ms, flip angle = 180°, resolution 640 × 448 pixels, field of view (FOV) = 120 × 82.5 mm^2. Signal intensities from regions of interest were manually measured by ImageJ software, and the T_2-relaxation time was calculated by fitting the signal from images with different TE. T_2-relaxivity values were calculated using a linear fitting of $1/T_2$ relaxation times to iron concentration. The slope of the fitting curve represents the R_2-value for MNCs covered with Pluronic F-127 used for MR imaging. The concentration of iron ions in each sample was determined using a standard ferrozine-based assay protocol.[27]

2.10. Characterization of MNCs by HERFD XANES. High energy resolution detected X-ray absorption spectra (HERFD XANES) of the Fe K-edge of MNCs were measured at the ID26 undulator beamline of the European Synchrotron Radiation Facility (ESRF). The incident energy was monochromized by Si(311) crystals. In order to measure HERFD-XANES spectra at the Fe K-edge, a set of four spherically bent Ge(440) crystals were used to deliver an Fe Kα1 emission line of maximum photons to the avalanche photodiode. The spectra were area normalized prior to analysis.

2.11. Characterization of Samples by FTIR Spectroscopy. FTIR spectra of samples were registered by means of a Nicolet 380 instrument (Thermo Scientific, USA), in KBr, in the range 400–4000 cm^{-1}. Infrared spectra were obtained by the KBr pellet method. In this method, the solid sample is finely pulverized with pure, dry KBr, the mixture is pressed in a hydraulic press to form a transparent pellet, and the spectrum of the pellet is measured.

3. RESULTS AND DISCUSSION

3.1. Synthesis of Magnetite Nanoclusters MNCs. Previously, two possible ways to prepare colloidal nanocrystal clusters were described: the two-step procedure that includes synthesis of individual nanoparticles (nanocrystals) and their

further aggregation in a controllable way[28,29] and the one-step protocol that combines the synthesis of nanoparticles and their aggregation into clusters.[30,31] In the present work, for the synthesis of colloidal nanocrystal clusters based on magnetic nanoparticles, we used the decomposition process of an iron-containing precursor such as iron(III) acetylacetonate in an organic medium (Scheme 1). In all cases, reaction parameters

**Scheme 1. Schematic Presentation of Synthesis of Colloidal Clusters**
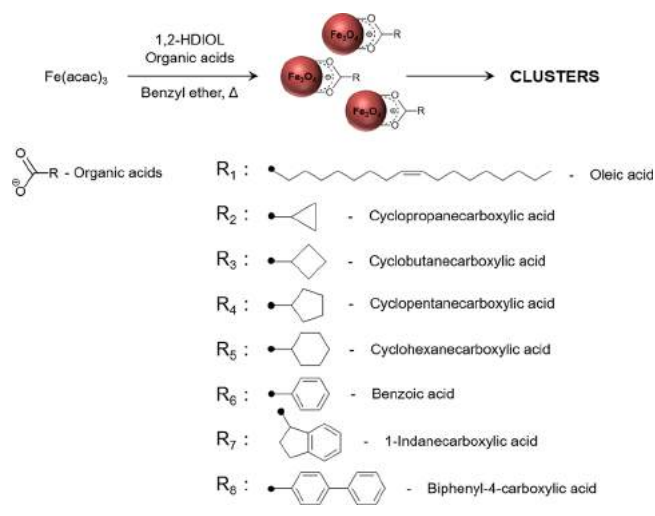
such as the amount of iron precursor and 1,2-HDIOL, temperature, heating, and stirring rate were identical, whereas the nature of the surfactants (organic acids) used for stabilization and shape control of MNCs during the synthesis process was different.

Previously, the effect of a bulky adamantane group on the formation of colloidal magnetite nanoclusters in the presence of 1-adamantanecarboxylic acid was described.[30] The effect of the structure and nature of the carboxylic acid substituent on the formation of MNCs was not clear until the end, as well as the mechanism of the MNC formation. Herein, for the first time, we used less hindered acids (cyclopropanecarboxylic, cyclo-butanecarboxylic, cyclopentanecarboxylic, cyclohexanecarbox-ylic, benzoic, biphenyl-4-carboxylic, and 1-indanecarboxylic) with pure alicyclic and aromatic fragments, as well as a mixed one (Table 1). Samples A, C, E, G, I, K, and M were prepared using a mixture of oleic acid (6 mmol) and another organic acid (6 mmol) (molar ratio = 1:1).

3.2. Characterization of MNCs by TEM and HRTEM. The size and morphology of the obtained samples were studied by TEM and HRTEM (Figure 1). From the TEM images, it was found that the samples A, B, D, F, J, K, and N represent cluster-like nanostructures with various shapes and structures of individual nanoparticles (Figure 1). Samples C, E, G, H, I, and M are faceted spheres with different sizes. The sample L is truncated cubes. Histograms of the size distribution of the obtained MNCs are presented in Figure S1.

It was discovered that the nature of the organic acid affects the morphology of individual magnetic nanoparticles as well as the structure of MNCs. Thereby, depending on the nature of the organic acid, we obtained nanomaterials with different structures. The formation mechanism of nanoclusters is not completely clear. As discussed in the literature, if the fusion of nanoparticles is prevented by separation with capping
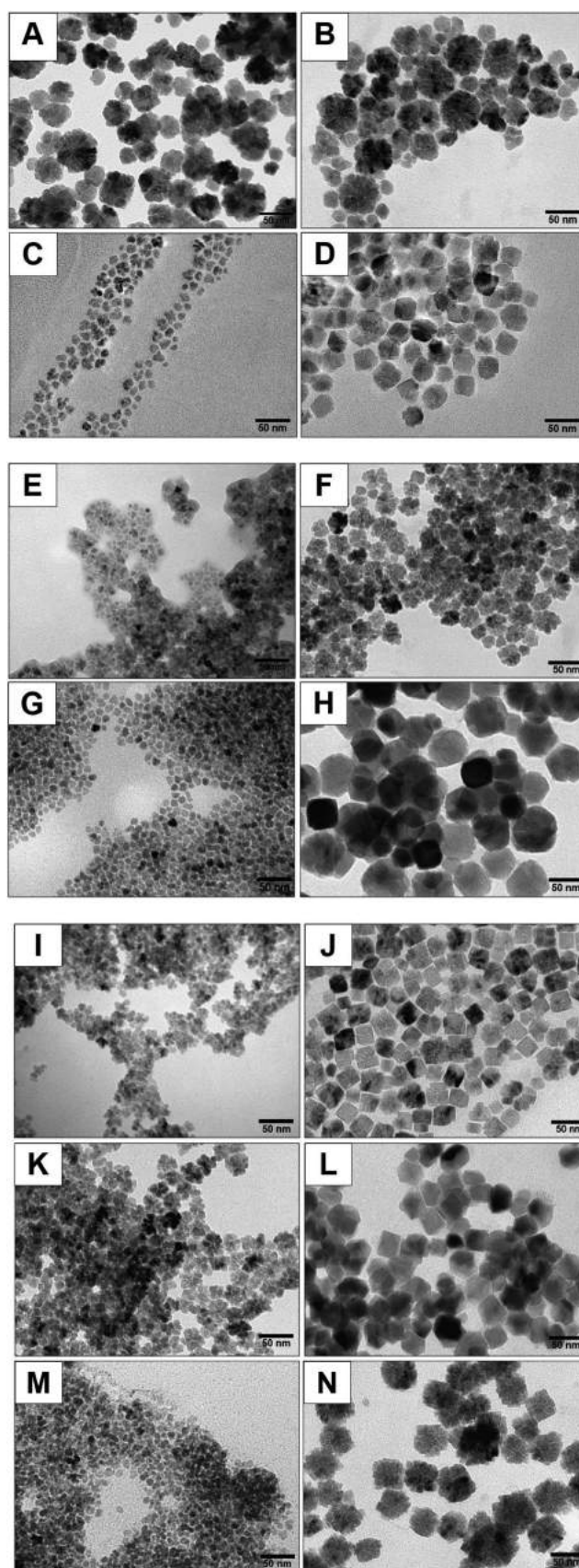
Figure 1. TEM images of synthesized samples.

molecules or other reasons, then mesocrystals are formed.[32] For example, Hugounenq et al.[33] synthesized iron oxide

nanoflowers in the presence of DEG and NMDEA. The structure of obtained nanoflowers contains defect holes. The authors suggest that such defect holes contain traces of solvents used for the synthesis (DEG and NMDEA) which are responsible for MNC formation.

We believe that in the case of MNCs A, B, D, F, J, K, and N nanocluster formation occurs from preobtained individual magnetic nanoparticles during the synthesis. The proof of formation is the presence of individual nanoparticles in TEM images as well as the clear distance between nanoparticles in the nanocluster. According to Fu's concept,[34] the key step of nanocluster formation is the adsorption−desorption process of organic ligands on the surface of initial nanoparticles. In Table 2, the basic characteristics of cyclocarboxylic acids used in the synthesis are presented.

Table 2. Basic Characteristics of Cyclocarboxylic Acids

acid	log P	boiling point (°C)
cyclopropanecarboxylic	0.48	182−184
cyclobutanecarboxylic	0.87	195
cyclopentanecarboxylic	1.26	216
cyclohexanecarboxylic	1.89	231−233
benzoic	1.87	249
1-indanecarboxylic	1.79	325
biphenyl-4-carboxylic	3.75	373
oleic	6.78	360

In the step of nucleation and growth of nanoparticles, the organic acid participates in multiple adsorption−desorption processes. Moreover, the amount of desorbed acid will be higher in the case of an organic acid having a greater affinity for the solvent—benzyl ether (log P = 3.95). Among all used cyclocarboxylic acids, cyclopropanecarboxylic acid has the lowest affinity to benzyl ether (Table 2). To investigate the effects of acid adsorption on growing seeds, we have additionally done synthesis in a mixture of organic acid and oleic acid in order to check if partial substitution by oleic acid will result in identical nanostructures. It is interesting that in the case of pure cyclopropanecarboxylic acid and a mixture of cyclopropanecarboxylic with oleic acid spherical clusters with identical structure and average size was obtained. Most probably initially nucleating seeds of iron oxide were stabilized by oleic and cyclocarboxylic acids. Then, cyclocarboxylic acid may be desorbed on free areas of nanoparticles or it can diffuse to the surface, displacing oleic acid. However, cyclopropanecarboxylic acid has the lowest value of log P = 0.48 among all aliphatic cyclocarboxylic acids and therefore it is firmly fixed to the surface of nanoclusters, whereas oleic acid is presented in solution.

The nature of cyclocarboxylic acids and values of log P affect the size and morphology of obtained nanoparticles. With increasing log P from cyclopropanecarboxylic acid to cyclohexanecarboxylic acid in the presence of oleic acid, we have not detected the formation of nanoclusterss. Cyclobutanecarboxylic acid molecules have a bigger size than cyclopropanecarboxylic acid molecules. Moreover, the value of log P for cyclobutanecarboxylic acid is 0.87, which is approximately 2 times larger than that for cyclopropanecarboxylic acid. Thus, cyclobutanecarboxylic acid molecules have more affinity to the solvent. In can be seen from Figure 1 that there are a lot of free nanoparticles with noncluster nature in sample C. Moreover, the crystallite size of sample C is less in comparison

with that of sample A, which can be explained by the fact that on the surface of particles more and more molecules of oleic acid are located, which prevent their subsequent adhesion with the formation of nanoclusters.

Cyclopentanecarboxylic and cyclohexanecarboxylic acids have even higher values of log P in comparison with cyclopropanecarboxylic acid (approximately 2 and 3 times, respectively). Thus, these acids are even less fixed on the surface of the particles and are easily replaced by oleic acid. Thereby, the diffusion of iron ions to the surface of growing crystals is complicated, which results in the formation of small nonclustered nanoparticles (samples E and G).

When pure cyclopropanecarboxylic acid (sample A) is used, cluster nanoparticles are formed from large crystallites due to the fact that this acid has a small molecule size and does not prevent diffusion of iron ions to the surface of growing nanoparticles. The same observation can be made in the case of cyclobutanecarboxylic acid (sample D). Cyclopentanecarboxylic acid (sample F) has a larger aliphatic tail that complicates the diffusion of Fe^{3+} ions, resulting in clusters having a smaller crystallite size. Cyclohexanecarboxylic acid having a higher value of log P = 1.89 is readily desorbed into the solution, and therefore, the surface of the nanoparticles becomes more available for Fe^{3+} ions. Thus, the diffusion of Fe^{3+} ions proceeds easily, which leads to the formation of large nanoparticles. A mixture of benzoic and 1-indacarboxylic acid with oleic acid results in a situation similar to the examples discussed above. Biphenyl-4-carboxylic acid has the highest value of log P = 3.75 among all cyclocarboxylic acids. In the case of pure biphenyl-4-carboxylic acid (sample L), cluster morphology is not observed due to the easy desorption of the acid to the solution.

To confirm that 1,2-HDIOL does not have an effect on the formation of nanoclusters, synthesis of MNCs only in the presence of 1,2-HDIOL and oleic acid was performed. As a result, only nanoparticles with a truncated sphere morphology were obtained (Supporting Information, Figure S2). All samples were synthesized under other heating rate conditions. As seen from TEM (Supporting Information, Figure S3), fast heating of the reaction mixture results in the formation of smaller MNCs. Previously, such an effect was observed during synthesis of magnetite nanoparticles and explained by the formation of a great number of magnetite seeds.[35] In contrast to most published MNC examples, all synthesized samples lie in the nanosized region. MNCs A and B have a similar structure and the same average size of nanoclusters. Among all synthesized MNCs, A, B, and N represent the most interest due to their clear cluster morphology. Thus, the most complete physicochemical studies were carried out for these MNCs.

More details about the structure of MNCs with unusual morphology were obtained from HRTEM (Figure 2). As we can see from HRTEM images of MNC A and MNC N, individual clusters randomly disoriented relatively to the direction of the primary beam, but inside they are composed of sufficiently perfect single-crystal particles with similar orientation (Figure 2(1),(2)). Also, from FFT images, it is clearly seen that the orientation of the particles in each cluster is very close (Figure 2(4),(5)).

The distance between two planes in individual particles in a specific direction is 0.297 nm, which is most likely the lattice spacing of (220) planes of the Fe_3O_4 phase (Figure 2(6)). MNCs A and N differ in shape and density. MNC N is more friable, and the particles are joined together to form voids. The shape of MNC A is close to spherical, and the shape of MNC N
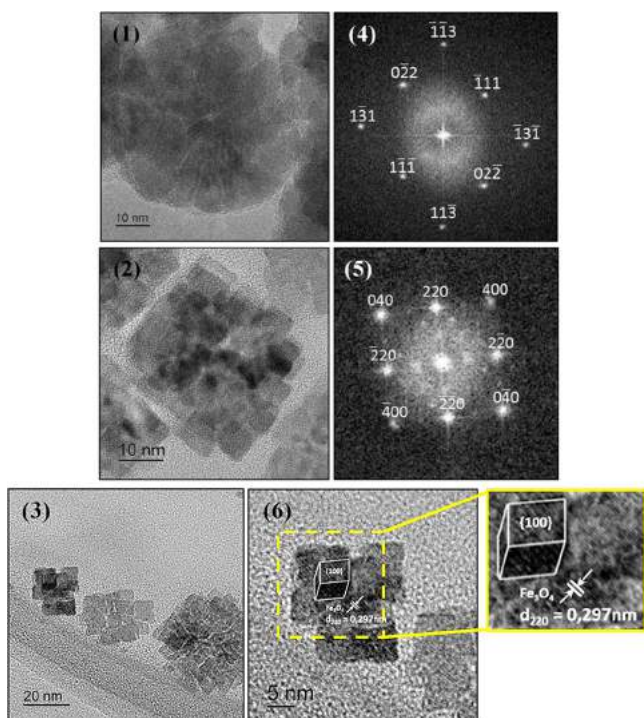
Figure 2. HRTEM images of (1) MNC A and (2) MNC N; cluster formation process for sample N (3); Fourier transform (FFT) images of (4) MNC A and (5) MNC N; (6) individual cubic particle of MNC N.

is close to cubic. Moreover, in the case of MNC N in Figure 2(3), it can be seen that the cluster growth process begins with aggregation of a small number of nanoparticles, which proves that the mechanism of MNC N formation is related to the self-assembling process.

By the way, some free nanoparticles were found in the final products (Figure 3), which argues that the MNCs were formed by oriented aggregation but not by splicing the individual particles with each other.
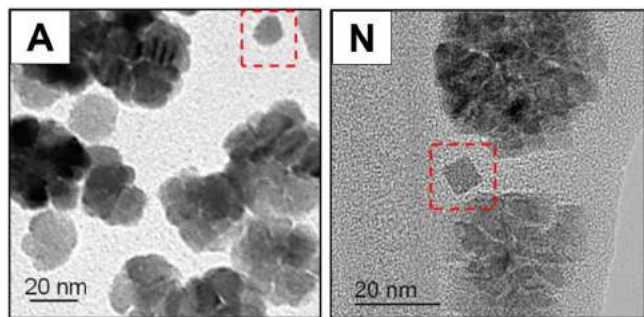

Figure 3. TEM images of individual magnetite nanoparticles (marked out area) in as-synthesized MNCs A and N.

Thus, we suggest that utilized acids are located in nanocluster defect holes and are attached to the surface of individual nanoparticles in a nanocluster. To confirm this suggestion, Fourier transform infrared (FTIR) spectroscopy for all obtained samples was performed (Figures 4−7). Figures 4 and 5 show the FTIR spectra of samples synthesized in the presence of pure aliphatic cyclocarboxylic acids (cyclopropane, cyclobutane, cyclopentane, and cyclohexanecaboxylic acids)
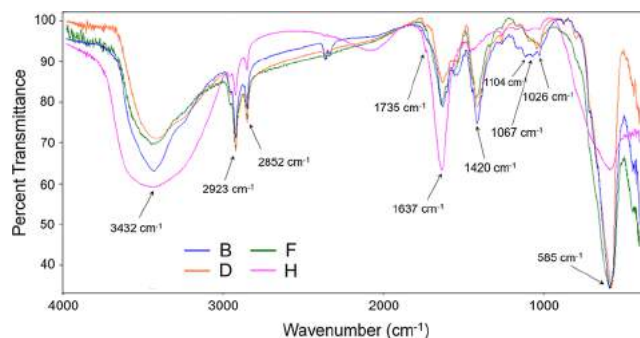
Figure 4. FTIR spectra of samples B, D, F, and H.
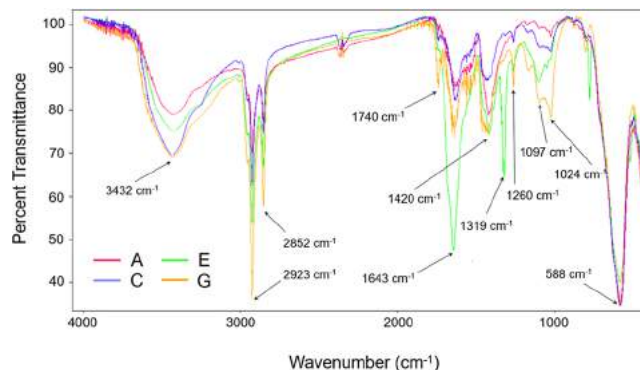
Figure 5. FTIR spectrum of magnetic nanoclusters.

and their mixture with oleic acid, respectively. The main bands at 585, 1420, 1637, 2852, 2923, and 3432 cm^{-1} have appeared in the FTIR spectrum of samples. In Figure 4, the band at 585 cm^{-1} corresponds to the vibration of the Fe−O bonds in all samples.[36] This band also occurs in all recorded spectra (Figures 4−7). The peaks of 1420 cm^{-1} are consistent with the stretching vibration of the carboxyl groups and occur in all cyclocarboxylic FTIR spectra.[37,38] In oleic acid, this band is present in the form of a doublet with similar intensities of each peak (1413 and 1458 cm^{-1}) (Supporting Information, Figure S4). The band at around 3432 cm^{-1} is attributed to the stretching modes of H_2O molecules which are most likely present in KBr. Also, the band at around 1635 cm^{-1} can be assigned to the bending vibrations of H_2O.[39] Furthermore, different peaks in the range 1026−1420 cm^{-1} confirm the presence of utilized cyclocarboxylic acids in MNCs (Supporting Information, Figure S5−S11). The peak at 1735 cm^{-1} corresponds to vibration of C=O stretching.

Comparing FTIR spectra of nanoparticles synthesized using pure aliphatic cyclocarboxylic acids with FTIR spectra of nanoparticles synthesized in the presence of a mixture of such acids with oleic acid, we can see an increase in the band intensity at 1097 cm^{-1} in the homologous series of aliphatic acids, starting with cyclopropanecarboxylic acid (Figure 5). This band is present in the FTIR spectrum of nanoparticles obtained in pure oleic acid (Supporting Information, Figure S12). As discussed above, with increasing size of aliphatic cyclocarboxylic acid, the cluster nature of the obtained samples disappears (samples A, C, E, and G).

In the case of pure benzoic, biphenyl-4-carboxylic, and 1-indanecarboxylic acids, it is also possible to observe characteristic bands of each acid. For example, in the case of biphenyl-4-carboxylic acid (sample L), we can observe characteristic bands from 1000 to 1200 cm^{-1} (two doublets and one singlet) which

is in good agreement with data obtained from the biphenyl-4-carboxylic FTIR spectrum. It should be noted that, because of the large number of peaks in the spectra of cyclic aromatic acids, it is difficult to establish any obvious changes in the spectra of samples synthesized with and without oleic acid addition (Figures 6 and 7).
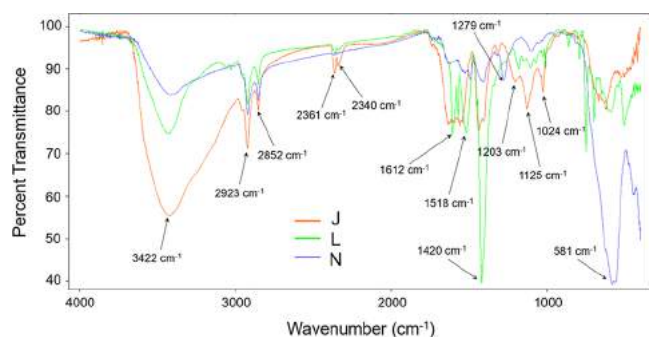

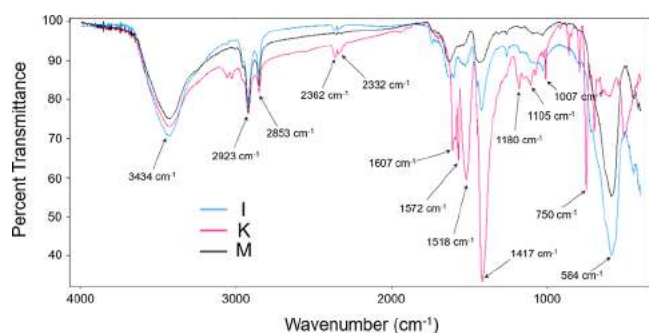**Figure 6.** FTIR spectrum of magnetic nanoclusters.

Figure 7. FTIR spectrum of magnetic nanoclusters.

3.3. XRD, Mössbauer Spectroscopy, and HERFD XANES of Samples.
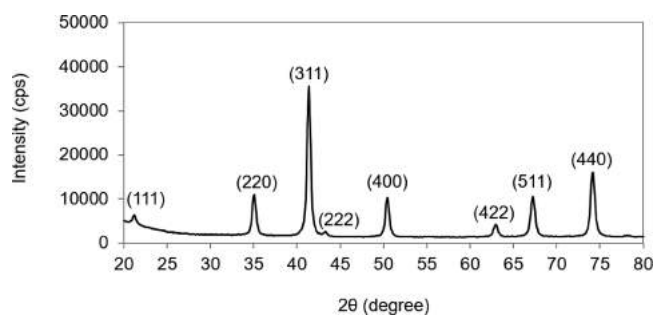The X-ray diffraction pattern of MNC A is shown in Figure 8. All synthesized MNCs have identical

Figure 8. XRD pattern of MNC A with the indexation of the Bragg peaks to an inverse spinel structure.

XRD patterns (Figure S13). The peaks can be indexed at 35.10, 41.41, 43.35, 50.48, 62.97, 67.28, and 74.18° corresponding to the crystal planes of {220}, {311}, {222}, {400}, {422}, {511}, and {440}, respectively.

The position and relative intensity of all diffraction peaks can be indexed to Fe_3O_4 ($a = 8.396$ Å, JCPDS no. 19-0629) or γ-Fe_2O_3 ($a = 8.346$ Å, JCPDS 39-1346) phases. XRD characteristics of the obtained MNCs are presented in Table 3.

It is well-known that according to the XRD data it is difficult to distinguish Fe_3O_4 and γ-Fe_2O_3 phases. In order to prove the

Table 3. XRD Characteristics of MNCs

	X-ray diffraction analysis		
	volume fraction (%)	crystallite size (nm)	lattice constants (nm)
sample	Fe_3O_4	Fe_3O_4	Fe_3O_4
A	100	18.4(3)	0.8392(6)
B	100	16.4(3)	0.8396(3)
D	100	13.3(4)	0.8387(3)
F	100	10.1(5)	0.8384(12)
J	100	15.9(3)	0.8407(18)
K	100	12.7(2)	0.8390(9)
N	100	10.8(5)	0.8399(10)

formation of the magnetite phase, the Mössbauer spectra for MNCs A and N are registered at room temperature. The recorded spectra have the form of asymmetric sextets (Figure 9).

Parameters of the hyperfine structure components of Mössbauer spectra are shown in Table S1. In order to describe the structure of MNCs more accurately, the calculation of obtained spectra was carried out (Table 4). As shown, the
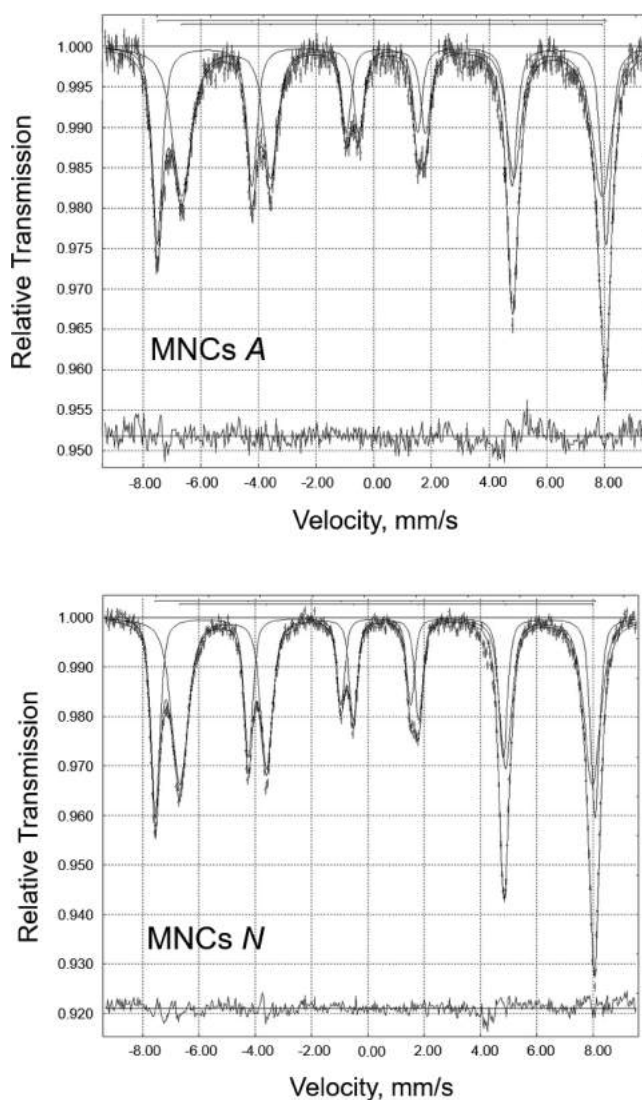

Figure 9. Room temperature Mössbauer spectra of MNC A and MNC N.

Table 4. Mössbauer Parameters Obtained from Experimental Spectra

MNCs	Mössbauer spectrum area of Fe^{3+} ions in tetrahedral site (S_a)	Mössbauer spectrum area of Fe^{2+} ions in octahedral site (S_b)	S_b/S_a (σ)	vacancy parameter (k)	Fe^{2+}/Fe (%)
A	35.78	64.22	1.7948	0.01	33
N	40.82	59.18	1.4498	0.04	30

Mössbauer spectra of the resulting materials confirm that the two sextuplets are due to the small difference between the hyperfine fields of the Fe^{3+} and Fe^{2+} ions in the sublattices for octahedral and tetrahedral sites. No signals due to the existence of other phases such as maghemite are observed.

The crystal-chemical formula for Fe_3O_4 can be written as $Fe^{3+}[Fe^{2+}_{1-3k}Fe^{3+}_{1+2k}\varphi_k]O_4$, where φ stands for a vacancy and k is a vacancy parameter. A feature of the Mössbauer spectra of nonstoichiometric magnetite is the distribution of the electron exchange between ions Fe^{3+} and Fe^{2+} in the octahedral positions in the presence of vacancies. At the same time, some of the Fe^{3+} ions, that are not involved in such exchanges because of the Fe^{2+} ion deficit, form a spectrum which is not distinguishable from a Mössbauer spectrum of Fe^{3+} ions in the tetrahedral positions. As a result, if we consider the probability of the resonance effect of iron ions in the tetrahedral and octahedral positions as equal, then the S_a/S_b ratio can be written as[40]

$$\sigma = \frac{S_b}{S_a} = \frac{2 - 6k}{1 + 5k}$$

S_a and S_b are Mössbauer spectra areas of Fe^{3+} ions in tetrahedral and octahedral sites, respectively.

Thereby, the vacancy parameter k can be calculated as

$$k = \frac{2 - \sigma}{6 + 5\sigma}$$

The vacancy parameter takes values equal to hundredths (Table 4) which means that all synthesized MNCs are pure magnetite.

Also, for MNCs A and N, the high energy resolution fluorescence detected X-ray absorption spectra (HERFD XANES) were registered. Fe K-edge XANES spectra are very sensitive to the electronic configuration of iron ions and are a direct probe of the oxidation state Fe^{2+} and Fe^{3+} ions. The latter could shed light on the iron oxide magnetic nanoparticle phase composition; particularly, it is capable of distinguishing between two spinel phases in small nanoparticles: magnetite and maghemite. Figure 10A shows HERFD XANES spectra of samples MNC N and MNC A in comparison to reference γ-Fe_2O_3 and Fe_3O_4.

It is clearly visible that MNC N is almost identical to Fe_3O_4; however, the MNC A spectrum shows a blue shift due to oxidation state. In order to obtain quantitative information on the electronic configuration of iron, a linear combination fit of reference sample spectra was performed. MNC A seems to be a mixture of Fe_3O_4 (91.8%) and γ-Fe_2O_3 (8.2%), while MNC N is almost totally Fe_3O_4 (99.6%). The remaining 0.4% refers to the phase γ-Fe_2O_3.

3.4. Magnetic Properties of MNCs. The main magnetic parameters of synthesized MNCs are reported in Table 5. Magnetic hysteresis measurements are carried out at 300 K and normalized to Fe_3O_4 content determined using TGA (Figure S14). The degradation of organic acids occurs in the range from
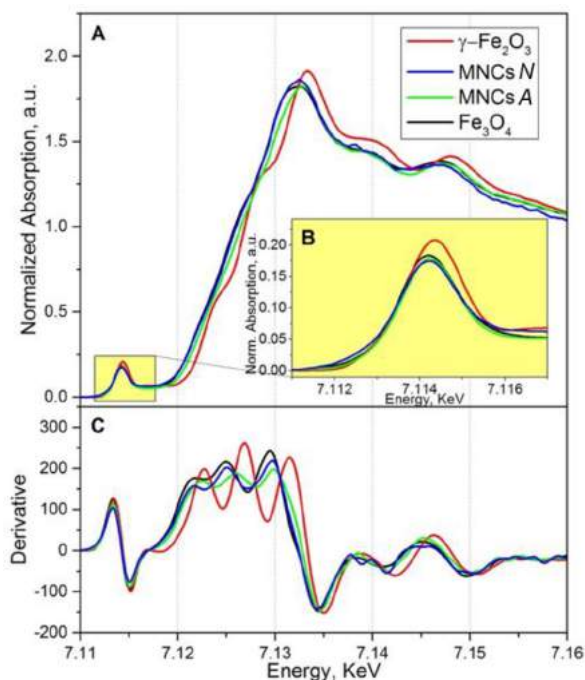
Figure 10. (A) HERFD XANES spectra of MNC A (green line) and MNC N (blue line) samples compared to reference Fe_3O_4 (black line) and γ-Fe_2O_3 (red line). (B) Pre-edge region of HERFD XANES spectra. (C) The first derivative of HERFD XANES spectra.

Table 5. Magnetic Parameters of Synthesized Samples

MNCs	size (nm)	crystallite size (nm)	magnetic properties		
			H_c (Oe)	M_r (emu/g)	M_s (emu/g)
K	23	12.7(2)	0.2	2.1	65.1
F	25	10.1(5)	9.0	0.9	78.1
D	31	13.3(4)	15.3	1.4	77.2
J	32	15.9(3)	17.5	1.6	77.8
N	38	10.8(5)	34.5	4.5	77.4
B	40	16.4(3)	49.0	4.3	80.5
A	41	18.4(3)	55.0	4.2	81.5

150 to 500 °C. Furthermore, degradation of all organic acids used in the synthesis of MNCs also takes place in this range. Weight reduction at the range above 500 °C is most likely due to the magnetite phase transformation processes.[41]

The hysteresis curves (M−H responses) for MNCs are shown in Figure 11.

Figure 11A indicates that all synthesized MNCs have relatively high saturation magnetization M_s values from 65.1 to 81.5 emu/g (for bulk magnetite, this value is 91 emu/g). These samples consist of magnetite nanoparticles with an average size from 10.1 to 18.4 nm (XRD analysis). High saturation magnetization of these samples can be explained by magnetostatic interactions between individual magnetite nanoparticles which lead to an increase of magnetic anisotropy of the nanoparticle complex.[42] Consequently, nanoparticles in the superparamagnetic state turn into the magnetically ordered state which increases saturation magnetization. Recently, Lee et al.[43] synthesized spherical MNCs with different sizes (from 16 to 512 nm) via a hydrolysis condensation and reductive polyol process and studied their magnetic properties. For example, for MNCs with a size of 32 nm, the values of coercivity and
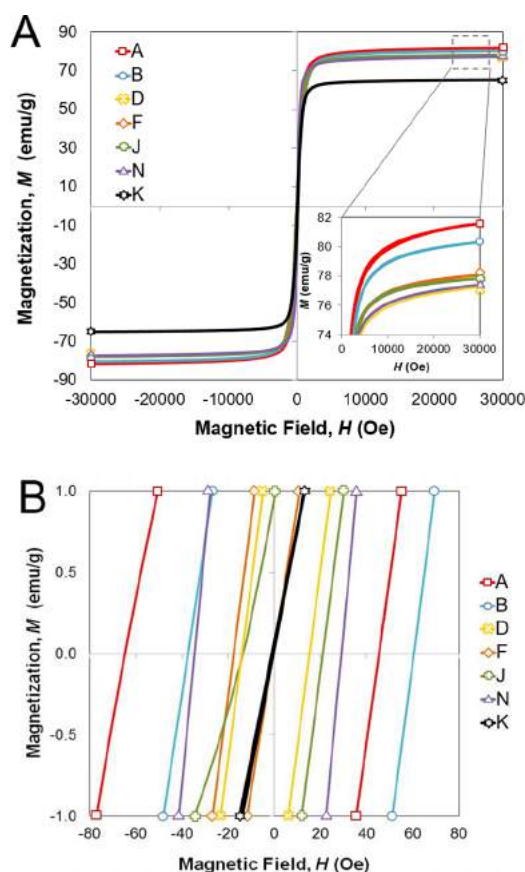
Figure 11. (A) Room temperature magnetization curves of MNCs obtained using a magnetic field from −30 to 30 kOe and (B) low-field portion showing H_c values.

magnetization were 0.57 Oe and 60.4 emu/g, respectively. In our case, MNC J with an average size of 32 nm has a coercivity of 17.5 Oe, while the magnetization is 77.8 emu/g. Moreover, the highest values of M_s (80.4 emu/g) in Lee's work were obtained for MNCs with a diameter of 422 nm. In our work, we obtained such magnetization for MNC B with a size of 40 nm. The maximum coercivity value was obtained for MNC A with a size of 41 nm (55 Oe), whereas the maximum coercivity in Lee's work was demonstrated for 123 nm MNCs. Figure 11B shows that MNCs are ferromagnetic at room temperature except for MNC K which are ferrimagnetic. The magnetic coercivity does not exceed 55.0 Oe for MNC A with an average size of 41 nm.

Figure 12 displays the H_c variation of MNCs as a function of their average size. The values of coercivity H_c increase with increasing size of MNCs as well as the values of saturation magnetization M_s, which is in agreement with previously published data for magnetic nanoclusters.[43]

3.5. MRI with Water-Soluble MNCs. MNCs A and N were transferred into aqueous medium by copolymer Pluronic F-127, and T_2 relaxivity was determined. For synthesis of water-soluble MNCs, they were conjugated with Pluronic F-127. We used Pluronic F-127 to decorate MNCs nanoparticles because it is a copolymer which consists of poly(ethylene oxide)−poly(propylene oxide)−poly(ethylene oxide) blocks. The hydrophilic corona prevents aggregation, protein adsorption, and RES recognition. Moreover, micelles based on Pluronic block copolymers can improve the sensitivity of multidrug resistant cancer cells to the anticancer chemotherapy.[44] The
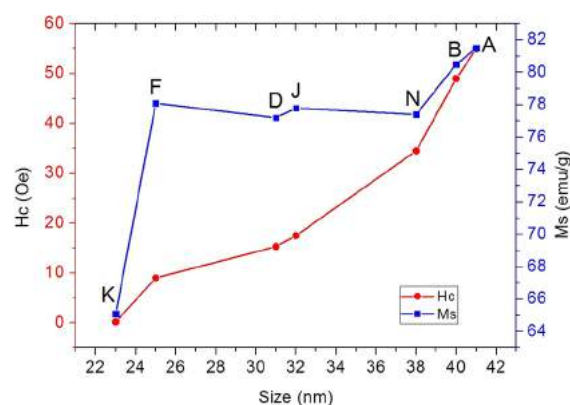
Figure 12. Curves of saturation magnetization (M_s) and coercive force (H_c) from the average size of samples obtained by TEM analysis.

results of size measurement using DLS show that the hydrodynamic diameter of the MNCs after coating with Pluronic F-127 is about 100 nm (Supporting Information, Figure S15). This is due to the fact that the MNCs are collected in small micelles. Plots of R_2 values and T_2-weighted MR images of MNCs at various concentrations of iron are presented in Figure 13.
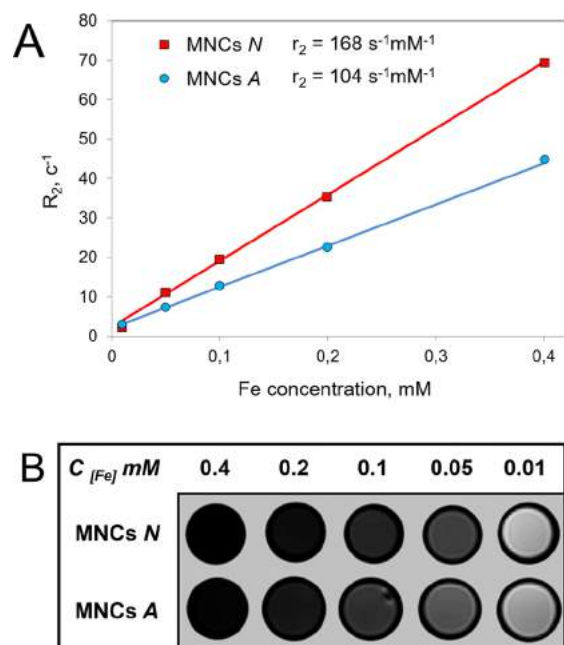
Figure 13. MR contrast effect of MNCs. (A) Plots of R_2 values of MNCs and (B) T_2-weighted MR images of MNCs at various concentrations of iron.

The T_2-weighted MR images show that MNC N has the most expressed T_2-contrast, compared with MNC A (Figure 13B). Probably, this fact can be explained by the cubic shape of MNPs consisting of MNCs. Lee and colleagues demonstrated very high r_2 values for cubic magnetite nanoparticles.[8] The r_2 values of MNC A and MNC N were 104 and 168 s^{-1} mM^{-1}, respectively. Compared with other MNCs (Table 6), we can conclude that our MNCs are very perspective materials for MRI investigations.

The smaller values of the T_2 relaxivity in comparison with previously obtained MNCs can be explained by the thickness of

Table 6. MNCs as Contrast Agents in MRI

clusters	nanocluster size (nm)	method	coating agent	r_2 (mM^{-1} s^{-1})
iron oxide[22]	13	TEM	poly(acrylic acid)	240
	36			540
iron oxide[45]	50	TEM	poly(dopamine)	160.68
γ-Fe$_2$O$_3$[46]	127	DLS	double hydrophilic copolymer (PAM-PTEA)	91
Fe$_3$O$_4$[47]	58	DLS	oleic acid (OA)/oleylamine in amphiphilic copolymer	117
densely packed SPIONs γ-Fe$_2$O$_3$/Fe$_3$O$_4$[48]	68	TEM	SDS	270
Fe$_3$O$_4$[49]	73	TEM	PLGA-PEG	333
MNC A (Fe$_3$O$_4$)	41	TEM	Pluronic F-127	104
MNC N (Fe$_3$O$_4$)	38	TEM	Pluronic F-127	168

the polymer shell. Previously, it was shown that increasing the size of the polymer shell leads to a decrease in the T_2 relaxivity values.[50] Pluronic F-127 has a large molecular weight (12 500 Da) and size which most likely leads to a decrease in T_2 relaxivity values. Nevertheless, the T_2 values of obtained MNCs are comparable with the T_2 values of commercial contrast agents based on iron oxide nanoparticles.[51] Thus, obtained MNCs are promising contrast agents for MRI investigations.

4. CONCLUSIONS

In this manuscript, we report a new one-step method for synthesis of MNCs based on thermal decomposition of iron precursor in the presence of different organic acids. The results show that the different organic acids can directly affect the final shape and size of the MNCs through the specific absorption onto the surface of magnetite nanocrystals. By this method, we obtained magnetite nanoclusters with different shapes and sizes. Using FTIR spectroscopy, we proved the presence of the organic acids in the structure of MNCs. Magnetic measurements of the obtained MNCs showed high saturation magnetization values (65.1−81.5 emu/g). MRI studies have revealed a high potential of Pluronic F-127 coated MNCs as T_2 contrast agents.

■ ASSOCIATED CONTENT

ⓢ Supporting Information

The Supporting Information is available free of charge on the ACS Publications website at DOI: 10.1021/acs.langmuir.8b00753.

Figure S1, histograms of the size distribution of obtained MNCs; Figure S2, TEM image of MNPs (13 ± 2 nm) synthesized in the presence of 1,2-HDIOL and oleic acid; synthesis of spherical MNCs with an average size of 21 nm; synthesis of cubic MNCs with an average size of 31 nm; Figure S3, TEM images of synthesized MNC A with average size 21 ± 3 nm and MNC N with average size 31 ± 8 nm; Figure S4, FTIR spectrum of oleic acid; Figure S5, FTIR spectrum of cyclopropanecarboxylic acid; Figure S6, FTIR spectrum of cyclobutanecarboxylic acid; Figure S7, FTIR spectrum of cyclopentanecarboxylic acid; Figure S8, FTIR spectrum of cyclohexanecarboxylic acid; Figure S9, FTIR spectrum of benzoic acid; Figure S10, FTIR spectrum of biphenyl-4-carboxylic acid; Figure S11, FTIR spectrum of 1-indanecarboxylic acid; Figure S12, nanoparticles obtained in the presence of pure oleic acid; Figure S13, XRD patterns of samples B, D, F, J, K, and N; Table S1, parameters of the hyperfine structure components obtained from the experimental Mössbauer spectra; Figure S14, TG curves of MNCs;

Figure S15, DLS measurements of MNCs A and N after conjugation with Pluronic F-127 (PDF)

■ AUTHOR INFORMATION

Corresponding Authors
*E-mail: nikitin.chemistry@mail.ru.
*E-mail: abakumov1988@gmail.com.

ORCID
Aleksey A. Nikitin: 0000-0002-9183-6713
Mikhail A. Soldatov: 0000-0003-1918-7875
Alexander G. Majouga: 0000-0002-5184-5551

Author Contributions
This manuscript was written through contribution of all authors. All authors have given approval to the final version of the manuscript.

Notes
The authors declare no competing financial interest.

■ REFERENCES

(1) Laurent, S.; Bridot, J.-L.; Elst, L. V.; Muller, R. N. Magnetic Iron Oxide Nanoparticles for Biomedical Applications. *Future Med. Chem.* **2010**, *2* (3), 427−449.

(2) Golovin, Y. I.; Gribanovsky, S. L.; Golovin, D. Y.; Klyachko, N. L.; Majouga, A. G.; Master, A. M.; Sokolsky, M.; Kabanov, A. V. Towards Nanomedicines of the Future: Remote Magneto-Mechanical Actuation of Nanomedicines by Alternating Magnetic Fields. *J. Controlled Release* **2015**, *219*, 43−60.

(3) Yang, H.; Liu, C.; Yang, D.; Zhang, H.; Xi, Z. Comparative Study of Cytotoxicity, Oxidative Stress and Genotoxicity Induced by Four Typical Nanomaterials: The Role of Particle Size, Shape and Composition. *J. Appl. Toxicol.* **2009**, *29* (1), 69−78.

(4) Xiong, Y.; Brunson, M.; Huh, J.; Huang, A.; Coster, A.; Wendt, K.; Fay, J.; Qin, D. The Role of Surface Chemistry on the Toxicity of Ag Nanoparticles. *Small* **2013**, *9* (15), 2628−2638.

(5) Tarantola, M.; Pietuch, A.; Schneider, D.; Rother, J.; Sunnick, E.; Rosman, C.; Pierrat, S.; Sönnichsen, C.; Wegener, J.; Janshoff, A. Toxicity of Gold-Nanoparticles: Synergistic Effects of Shape and Surface Functionalization on Micromotility of Epithelial Cells. *Nanotoxicology* **2011**, *5* (2), 254−268.

(6) Sun, S.; Zeng, H. Size-Controlled Synthesis of Magnetite Nanoparticles. *J. Am. Chem. Soc.* **2002**, *124* (28), 8204−8205.

(7) Park, J.; An, K.; Hwang, Y.; Park, J.-G.; Noh, H.-J.; Kim, J.-Y.; Park, J.-H.; Hwang, N.-M.; Hyeon, T. Ultra-Large-Scale Syntheses of Monodisperse Nanocrystals. *Nat. Mater.* **2004**, *3* (12), 891−895.

(8) Lee, N.; Choi, Y.; Lee, Y.; Park, M.; Moon, W. K.; Choi, S. H.; Hyeon, T. Water-Dispersible Ferrimagnetic Iron Oxide Nanocubes with Extremely High R 2 Relaxivity for Highly Sensitive in Vivo MRI of Tumors. *Nano Lett.* **2012**, *12* (6), 3127−3131.

(9) Hai, H. T.; Yang, H. T.; Kura, H.; Hasegawa, D.; Ogata, Y.; Takahashi, M.; Ogawa, T. Size Control and Characterization of Wustite (Core)/spinel (Shell) Nanocubes Obtained by Decomposition of Iron Oleate Complex. *J. Colloid Interface Sci.* **2010**, *346* (1), 37−42.

(10) Abbas, M.; Takahashi, M.; Kim, C. Facile Sonochemical Synthesis of High-Moment Magnetite (Fe 3O4) Nanocube. *J. Nanopart. Res.* **2013**, *15* (1), 1354.

(11) Xu, Y.; Sherwood, J.; Qin, Y.; Holler, R. A.; Bao, Y. A General Approach to the Synthesis and Detailed Characterization of Magnetic Ferrite Nanocubes. *Nanoscale* **2015**, *7* (29), 12641−12649.

(12) Xu, X.; Friedman, G.; Humfeld, K. D.; Majetich, S. A.; Asher, S. A. Synthesis and Utilization of Monodisperse Superparamagnetic Colloidal Particles for Magnetically Controllable Photonic Crystals. *Chem. Mater.* **2002**, *14* (3), 1249−1256.

(13) Ge, J.; Hu, Y.; Biasini, M.; Beyermann, W. P.; Yin, Y. Superparamagnetic Magnetite Colloidal Nanocrystal Clusters. *Angew. Chem., Int. Ed.* **2007**, *46* (23), 4342−4345.

(14) Kostopoulou, A.; Lappas, A. Colloidal Magnetic Nanocrystal Clusters: Variable Length-Scale Interaction Mechanisms, Synergetic Functionalities and Technological Advantages. *Nanotechnol. Rev.* **2015**, *4*, 595−624.

(15) Barick, K. C.; Aslam, M.; Lin, Y.-P.; Bahadur, D.; Prasad, P. V.; Dravid, V. P. Novel and Efficient MR Active Aqueous Colloidal Fe3O4 Nanoassemblies. *J. Mater. Chem.* **2009**, *19* (38), 7023.

(16) Li, M.; Gu, H.; Zhang, C. Highly Sensitive Magnetite Nano Clusters for MR Cell Imaging. *Nanoscale Res. Lett.* **2012**, *7*, 204.

(17) Dong, F.; Guo, W.; Bae, J. H.; Kim, S. H.; Ha, C. S. Highly Porous, Water-Soluble, Superparamagnetic, and Biocompatible Magnetite Nanocrystal Clusters for Targeted Drug Delivery. *Chem. - Eur. J.* **2011**, *17* (45), 12802−12808.

(18) Deng, H.; Li, X.; Peng, Q.; Wang, X.; Chen, J.; Li, Y. Monodisperse Magnetic Single-Crystal Ferrite Microspheres. *Angew. Chem., Int. Ed.* **2005**, *44* (18), 2782−2785.

(19) Xuan, S.; Wang, Y.-X. J.; Yu, J. C.; Cham-Fai Leung, K. Tuning the Grain Size and Particle Size of Superparamagnetic Fe 3 O 4 Microparticles. *Chem. Mater.* **2009**, *21*, 5079−5087.

(20) Fan, T.; Pan, D.; Zhang, H. Study on Formation Mechanism by Monitoring the Morphology and Structure Evolution of Nearly Monodispersed Fe3O4 Submicroparticles with Controlled Particle Sizes. *Ind. Eng. Chem. Res.* **2011**, *50* (15), 9009−9018.

(21) Xu, F.; Cheng, C.; Xu, F.; Zhang, C.; Xu, H.; Xie, X.; Yin, D.; Gu, H. Superparamagnetic Magnetite Nanocrystal Clusters: A Sensitive Tool for MR Cellular Imaging. *Nanotechnology* **2009**, *20* (40), 405102.

(22) Xu, F.; Cheng, C.; Chen, D. X.; Gu, H. Magnetite Nanocrystal Clusters with Ultra-High Sensitivity in Magnetic Resonance Imaging. *ChemPhysChem* **2012**, *13* (1), 336−341.

(23) Maity, D.; Chandrasekharan, P.; Pradhan, P.; Chuang, K.-H.; Xue, J.-M.; Feng, S.-S.; Ding, J. Novel Synthesis of Superparamagnetic Magnetite Nanoclusters for Biomedical Applications. *J. Mater. Chem.* **2011**, *21* (38), 14717.

(24) Lartigue, L.; Hugounenq, P.; Alloyeau, D.; Clarke, S. P.; Lévy, M.; Bacri, J. C.; Bazzi, R.; Brougham, D. F.; Wilhelm, C.; Gazeau, F. Cooperative Organization in Iron Oxide Multi-Core Nanoparticles Potentiates Their Efficiency as Heating Mediators and MRI Contrast Agents. *ACS Nano* **2012**, *6* (12), 10935−10949.

(25) Luo, B.; Xu, S.; Luo, A.; Wang, W. R.; Wang, S. L.; Guo, J.; Lin, Y.; Zhao, D. Y.; Wang, C. C. Mesoporous Biocompatible and Acid-Degradable Magnetic Colloidal Nanocrystal Clusters with Sustainable Stability and High Hydrophobic Drug Loading Capacity. *ACS Nano* **2011**, *5* (2), 1428−1435.

(26) Cho, M.; Cervadoro, A.; Ramirez, M.; Stigliano, C.; Brazdeikis, A.; Colvin, V.; Civera, P.; Key, J.; Decuzzi, P. Assembly of Iron Oxide Nanocubes for Enhanced Cancer Hyperthermia and Magnetic Resonance Imaging. *Nanomaterials* **2017**, *7* (4), 72.

(27) Riemer, J.; Hoepken, H. H.; Czerwinska, H.; Robinson, S. R.; Dringen, R. Colorimetric Ferrozine-Based Assay for the Quantitation of Iron in Cultured Cells. *Anal. Biochem.* **2004**, *331* (2), 370−375.

(28) Mehdizadeh Taheri, S.; Michaelis, M.; Friedrich, T.; Förster, B.; Drechsler, M.; Römer, F. M.; Bösecke, P.; Narayanan, T.; Weber, B.; Rehberg, I.; et al. Self-Assembly of Smallest Magnetic Particles. *Proc. Natl. Acad. Sci. U. S. A.* **2015**, *112* (47), 14484−14489.

(29) Kralj, S.; Makovec, D. Magnetic Assembly of Superparamagnetic Iron Oxide Nanoparticle Clusters into Nanochains and Nanobundles. *ACS Nano* **2015**, *9* (10), 9700−9707.

(30) Zhang, L.; Dou, Y. H.; Gu, H. C. Sterically Induced Shape Control of Magnetite Nanoparticles. *J. Cryst. Growth* **2006**, *296* (2), 221−226.

(31) Töpfer, J.; Angermann, A. Nanocrystalline Magnetite and Mn-Zn Ferrite Particles via the Polyol Process: Synthesis and Magnetic Properties. *Mater. Chem. Phys.* **2011**, *129* (1−2), 337−342.

(32) Lu, Z.; Yin, Y. Colloidal Nanoparticle Clusters: Functional Materials by Design. *Chem. Soc. Rev.* **2012**, *41* (21), 6874.

(33) Hugounenq, P.; Levy, M.; Alloyeau, D.; Lartigue, L.; Dubois, E.; Cabuil, V.; Ricolleau, C.; Roux, S.; Wilhelm, C.; Gazeau, F.; et al. Iron Oxide Monocrystalline Nanoflowers for Highly Efficient Magnetic Hyperthermia. *J. Phys. Chem. C* **2012**, *116* (29), 15702−15712.

(34) Fu, J.; He, L.; Xu, W.; Zhuang, J.; Yang, X.; Zhang, X.; Wu, M.; Yin, Y.; Murray, C. B.; Kagan, C. R.; et al. Formation of Colloidal Nanocrystal Clusters of Iron Oxide by Controlled Ligand Stripping. *Chem. Commun.* **2016**, *52* (1), 128−131.

(35) Guardia, P.; Pérez-Juste, J.; Labarta, A.; Batlle, X.; Liz-Marzán, L. M. Heating Rate Influence on the Synthesis of Iron Oxide Nanoparticles: The Case of Decanoic Acid. *Chem. Commun.* **2010**, *46* (33), 6108.

(36) Waldron, R. D. Infrared Spectra of Ferrites. *Phys. Rev.* **1955**, *99* (6), 1727−1735.

(37) Kouassi, G. K.; Irudayaraj, J.; McCarty, G. Activity of Glucose Oxidase Functionalized onto Magnetic Nanoparticles. *Biomagn. Res. Technol.* **2005**, *3*, 1.

(38) Dallas, P.; Georgakilas, V.; Niarchos, D.; Komninou, P.; Kehagias, T.; Petridis, D. Synthesis, Characterization and Thermal Properties of Polymer/magnetite Nanocomposites. *Nanotechnology* **2006**, *17* (8), 2046−2053.

(39) Zhang, Z. J.; Chen, X. Y.; Wang, B. N.; Shi, C. W. Hydrothermal Synthesis and Self-Assembly of Magnetite (Fe3O4) Nanoparticles with the Magnetic and Electrochemical Properties. *J. Cryst. Growth* **2008**, *310* (24), 5453−5457.

(40) Voleník, K.; Seberíni, M.; Neid, J. A Mössbauer and X-Ray Diffraction Study of Nonstoichiometry in Magnetite. *Czech. J. Phys.* **1975**, *25* (9), 1063−1071.

(41) Yang, K.; Peng, H.; Wen, Y.; Li, N. Re-Examination of Characteristic FTIR Spectrum of Secondary Layer in Bilayer Oleic Acid-Coated Fe3O4 nanoparticles. *Appl. Surf. Sci.* **2010**, *256* (10), 3093−3097.

(42) Caruntu, D.; Caruntu, G.; O'Connor, C. J. Magnetic Properties of Variable-Sized Fe3O4 Nanoparticles Synthesized from Non-Aqueous Homogeneous Solutions of Polyols. *J. Phys. D: Appl. Phys.* **2007**, *40* (19), 5801−5809.

(43) Lee, J. S.; Cha, J. M.; Yoon, H. Y.; Lee, J. K.; Kim, Y. K. Magnetic Multi-Granule Nanoclusters: A Model System That Exhibits Universal Size Effect of Magnetic Coercivity. *Sci. Rep.* **2015**, *5*, 12135.

(44) Batrakova, E. V.; Kabanov, A. V. Pluronic Block Copolymers: Evolution of Drug Delivery Concept from Inert Nanocarriers to Biological Response Modifiers. *J. Controlled Release* **2008**, *130*, 98−106.

(45) Wu, M.; Zhang, D.; Zeng, Y.; Wu, L.; Liu, X.; Liu, J. Nanocluster of Superparamagnetic Iron Oxide Nanoparticles Coated with Poly (Dopamine) for Magnetic Field-Targeting, Highly Sensitive MRI and Photothermal Cancer Therapy. *Nanotechnology* **2015**, *26* (11), 115102.

(46) Vuong, Q. L.; Berret, J. F.; Fresnais, J.; Gossuin, Y.; Sandre, O. A Universal Scaling Law to Predict the Efficiency of Magnetic

Nanoparticles as MRI T2-Contrast Agents. *Adv. Healthcare Mater.* **2012**, *1* (4), 502−512.

(47) Xie, X.; Zhang, C. Controllable Assembly of Hydrophobic Superparamagnetic Iron Oxide Nanoparticle with mPEG-PLA Copolymer and Its Effect on MR Transverse Relaxation Rate. *J. Nanomater.* **2011**, *2011*, 152524.

(48) Paquet, C.; De Haan, H. W.; Leek, D. M.; Lin, H. Y.; Xiang, B.; Tian, G.; Kell, A.; Simard, B. Clusters of Superparamagnetic Iron Oxide Nanoparticles Encapsulated in a Hydrogel: A Particle Architecture Generating a Synergistic Enhancement of the T2relaxation. *ACS Nano* **2011**, *5* (4), 3104−3112.

(49) Yang, J.; Lee, C. H.; Ko, H. J.; Suh, J. S.; Yoon, H. G.; Lee, K.; Huh, Y. M.; Haam, S. Multifunctional Magneto-Polymeric Nanohybrids for Targeted Detection and Synergistic Therapeutic Effects on Breast Cancer. *Angew. Chem., Int. Ed.* **2007**, *46* (46), 8836−8839.

(50) Chen, Y. J.; Tao, J.; Xiong, F.; Zhu, J. B.; Gu, N.; Geng, K. K. Characterization and in Vitro Cellular Uptake of PEG Coated Iron Oxide Nanoparticles as MRI Contrast Agent. *Pharmazie* **2010**, *65* (7), 481−486.

(51) Wang, Y.-X. J. Superparamagnetic Iron Oxide Based MRI Contrast Agents: Current Status of Clinical Application. *Quant. Imaging Med. Surg* **2011**, *1* (Dcc), 35−44.